Design optimization and structural assessment of a header and coil steam generator for load-following solar tower plants

P.A. González-Gómez*, M. Laporte-Azcué , M. Fernández-Torrijos , D. Santana

Energy Systems Engineering Group (ISE), Department of Thermal and Fluid Engineering, University Carlos III of Madrid, Av. Universidad 30, 28911, Leganés, Madrid, Spain

A B S T R A C T

The aim of this work is to explore the capabilities, from heat transfer and structural point of view, of a novel header and coil steam generator for a 100 MWe solar tower plant using molten-salt as heat transfer fluid. A methodology for the design and economic optimization of the header and coil steam generator is presented, paying special attention to the structural assessment which considers complex phenomena such creep-fatigue and stress relaxation due to the high working temperatures of solar tower plants. The results showed that header and coil steam generators provide economically effective overall heat transfer coefficients with lower pressure drops on the shell side compared to conventional shell-and-tube steam generators, leading to a reduction in the annual pumping costs of around 3.6 times. The structural assessment reveals that the critical points are located in the headers of superheater, reheater and evaporator. Different redesign actions have been performed to increase the lifetime in the critical points without affecting to the optimum thermo-economic solutions. Finally, the results showed that the header and coil steam generator is able to operate with fast daily startups at 6.1 K/min, a ramp-up 2.4 times higher than conventional shell-and-tube steam generators.

© 2022 The Authors. Published by Elsevier Ltd. This is an open access article under the CC BY-NC-ND license (http://creativecommons.org/licenses/by-nc-nd/4.0/).

1. Introduction

Concentrating solar power (CSP) plants have two main distinctive features compared to variable renewable energy sources like wind or photovoltaics: i) Higher operational value (due to the avoided costs of conventional generation at their respective dispatching times, related with ancillary services costs) and ii) Higher capacity value (which refers to the costs avoided due to building new conventional generation as a response to the growth on the energy demand) [1]. Despite CSP plants with thermal energy storage have higher cost per unit of energy produced, they present additional economic value due to their higher capacity factors and their possibility to participate in grid balancing services (grid balancing, spinning reserve, ancillary services, etc).

Throughout the last decade, the generation costs of photovoltaics have diminished dramatically. As a result, it is expected that CSP plants will work as load following plants, generating electricity early in the morning and late in the afternoon, while photovoltaics will provide electricity during the day [2]. Among the CSP technologies, the solar tower one excels the rest with its lowest generation costs. However, solar tower plants (STPs) are not fully developed technologically, and therefore it is not clear whether this operation mode fully increases its competitiveness due to the resulting growth of costs related to cyclic operation. Effectively, the equipment responsible for the electricity generation, such as the steam generator (SG) or the steam turbine systems, will be exposed to strong cycling conditions, thus facing an increase of the failure rates.

Different works related to the design of the steam generators for CSP plants can be found in the literature. González-Gómez et al. [3,4] performed the design and optimization of the steam generators for parabolic and tower solar plants based on conventional shell-and-tube heat exchangers. The Stream Analysis method [5], which considers the different flow streams through the complex geometry on the shell side, was used to estimate the heat transfer coefficient and the pressure drop. Due to the large number of design variables, an optimization method was developed based on genetic algorithms and using several constraints according to good design practices recommendations of conventional shell-and-tube exchangers. Focusing on steam generators for STPs, a complete study can be found in Ref. [6]. In this work, four SG designs for a

* Corresponding author.
E-mail address: pegonzal@ing.uc3m.es (P.A. González-Gómez).

Nomenclature

Abbreviations

ASME	American Society of Mechanical Engineers
CT	Cold Tank
CSP	Concentrated solar power
EPC	Engineering, procurement and construction
EV	Evaporator
FW	Feed water
HP	High pressure
HT	Hot tank
HTF	Heat transfer fluid
HX	Heat exchanger
LP	Low pressure
NREL	National Renewable Energy Laboratory
PH	Preheater
R	Receiver
RH	Reheater
SG	Steam Generator
SH	Superheater
STP	Solar tower plant
TAC	Total annualized cost (€)

Symbols

A	area (m^2)
a	convective coefficient constants for a tube bank in cross flow
b	heat exchanger base cost (€/m^2), pressure drop constants for a tube bank in cross flow
C	cost (€), additional tube thickness (mm)
CE_{index}	Chemical Engineering Plant Cost Index
C_k	notch factor
C_p	specific heat capacity (J/Kg K), plasticity correction factor
C_{T*}	temperature correction factor
c	cost correction factor, creep strain rate model constants
D	outer diameter (m)
D_c	creep damage
D_f	fatigue damage
D_L	damage limit
d	inner diameter (m)
E	Young modulus (MPa), joint efficiency
F	temperature correction factor
f	friction factor, front head correction factor
f_{rc}	capital return factor
G	mass flux (kg/s m^2)
H	Hours of operation (hours), dwell time period (hours)
h	heat transfer coefficient (W/m^{2}K)
j	cross flow coefficient
K	strain hardening parameter (MPa), loss coefficient
K_{hor}	heat flux correction factor
K_{safe}	creep damage safety factor
k	thermal conductivity (W/mK)
L	length (m)
M	total number of cycles
$\dot{m}$	mass flow rate (kg/s)
N_A	number of allowable cycles
N_x	number of tube rows
N_y	number of tube columns

n	strain hardening exponent
n_{year}	lifetime (years)
P	pressure (Pa)
Pr	Prandtl number
R_m	ultimate tensile strength (MPa)
T	Temperature (°C)
t	thickness (m), time (s)
p_t	tube pitch (m)
p	outer tube diameter cost multiplier
Q	heat (W)
q''	heat flux (W/m2)
S	ASME allowable stress (MPa)
S_H	hot relaxation strength (MPa)
S_y	yield strength (MPa)
$S_{y,c}$	yield strength at the cold cycle (MPa)
Re	Reynolds Number
R	outer radius (m)
r	inner radius(m), radial direction (m), rear header correction factor
t_R	time to rupture (hours)
U	overall heat transfer coefficient (W/m^{2}K)
u	velocity (m/s)
X	normalized pressure stress
Y	normalized thermal stress
y	temperature coefficient
Z	normalized lower bound stress

Greek Symbols

ΔT_{lm}	log mean temperature difference (°C)
α	stress concentration factor, thermal diffusivity (m^2/s)
β	thermal expansion coefficient (K^{-1})
θ	angle (rad)
ρ	density (kg/m^3)
η	efficiency
μ	absolute viscosity (mPa·s)
ν	Poisson's ratio
σ	stress (MPa)
σ_{fa}	corrected stress range (MPa)
ε	strain
$\dot{\varepsilon}_c$	creep strain rate (1/hours)
ε_{offset}	strain offset
φ	viscosity correction factor

Subscripts

b	bend
$bank$	tube bank
cap	capital
$cont$	contraction
$crit$	critical
e	electricity
eff	effective
exp	expansion
$head$	header
hor	horizontal
i	inner
LB	lower bound
M	mechanical
m	mean
max	maximum
o	outer
$nozzle$	nozzle

pump	pumping		Superscripts	
ref	reference		creep	creep
s	shell		E	Elastic
T	thermal		relax	relaxation
t	tube			
ver	vertical			

100MWe commercial plant proposed by different vendors were analyzed. Foster Wheeler proposed a straight tube/straight shell heat exchanger with the molten-salt placed on the shell side, forcing the need of using floating head. Struthers Wells and ABB Lummus presented a very similar design which consists of a U-tube kettle boiler and U-tube/straight shell heat exchangers. Lastly, the Babcock and Wilcox design consisted of U-tube/U-shell heat exchangers with the molten-salt placed on the shell side. The main advantage of the U-shell design was the elimination of the thermal stresses originated in the tubesheet diametral lane. In a recent study [7], developed by the German Aerospace Center (DLR) in collaboration with other private companies, a series of design guidelines for a new generation of STP of 200 MWe were proposed. Different designs for a natural circulation SG such as U-tube, straight-tube and header-type are briefly analyzed. Additionally, a once-through SG design concept is presented, studying its main advantages such as: higher ramp rates during startup (up to 10 K/min), and lower number of vessels, pipes and valves than natural circulation SG. However, the once-through SG was not selected as the most suitable alternative due to the higher complexity of reparation and/or replacement tasks compared to the natural circulation SG. Finally, the design selected for the SG consisted of U-tube shell-and-tube heat exchangers mainly due to the low cost.

In a near future it is expected that the operation of CSP plants will be rather cyclic and thus the evaluation against cyclic operation of the SG is mandatory to guarantee reliable designs. The high working temperatures of molten-salt SG (~565 °C) induce creep damage and therefore complex phenomena such as creep-fatigue combination may occur, having a significant impact on its lifetime. This issue is addressed in several standards such as ASME code, European Standard (EN-13445) or British Standard R5. In the literature a few works related to this topic can be found. For example, Gonzalez-Gomez et al. [8] analyzed the lifetime of a SG based on conventional shell-and-tube heat exchangers, considering both baseload and cycling operation conditions for a STP, following the ASME Section III Subsection NH code [9]. Finite element simulations were carried out for different exchangers points for accurate stress estimations. The maximum allowable temperature ramp rate for a daily startup was estimated to be 2.5 K/min. Agnetti [2] performed a lifetime analysis of a SG of a 100 MWe STP using an innovative concept of heat exchangers specifically designed for cycling operation. Finite element simulations were performed based on inelastic approach and following ASME Section III Subsection NH code [9]. The results showed that the proposed SG design was able to operate more than 200 000 h and 25 000 cycles without creep-fatigue failure. However, details of the heat exchangers geometry and material models for the finite element modeling were not shown. In Ref. [10] analyzed the reliability of a STP operated at strong cyclic conditions where the cycling cost and the forced outages were estimated considering the failures on the SG.

The analysis of the dynamic operations such as startups or load changes is a recommended practice for the complete evaluation of a steam generator design at issue. For example, Zhang et al. [11] studied the dynamic operation of the molten-salt steam generator of Solar Two power plant. Different load change operations that can occur in solar tower plants were analyzed where the transient responses and time constants of the steam generator fluids were obtained. Li et al. [12] carried out a dynamic model of an oil/water steam generator based on the lumped parameter method. A control scheme was developed and checked against different disturbance cases in steam generation systems. Soares et al. [13] performed a quasi-dynamic model for a once-through direct steam generation system in parabolic trough solar collectors. The model results were compared against experimental data for different operation processes such as start-up, cool-down, steady and transient solar radiation.

A recent study presented by the National Renewable Energy Laboratory (NREL) [14] gathers data from a high number of participants involved in the CSP industry such us plant owners, operators, engineering, procurement, and construction (EPC) contractors. Such document highlights that the reliability of the SG has been the most noted issue regarding the availability of both trough and molten-salt tower plants. Additionally, the final results of the survey reveal that the main concern evaluated for the participants was the SG reliability, which is first in the list, above issues that occurred in other systems such as the storage system or the central receiver. It should be noted that the design of the SG of many operating CSP plants is based on conventional shell-and-tube heat exchangers where the main causes of forced outages are failures of the tube-to-tubesheet connections, which produce steam/water leakage into the heat transfer fluid circuit. In Ref. [14] it is mentioned the possibility of using the header and coil heat exchangers instead of the common shell-and-tube design because they are experiencing lower failure rates. Nevertheless, it is also remarked that there are not enough header and coil heat exchangers in service to develop a reliable database.

In contrast to conventional shell-and-tubes, works related to header and coil heat exchangers are scarce in the literature. For example, Ferruzza et al. [15] proposed a methodology for the design of header and coil SG according to ASME Section I [16] and the EN 12952-3 [17]. They suggested that the integration of the low-cycle fatigue constraints during the thermo-economic optimization phase is a highly recommended practice. The heat exchanger geometry was optimized for a parabolic trough solar power plant by minimizing the total heat transfer fluid pressure drop and investment costs while considering required heating rates at the same time. A later work presented by the authors [18] completed the methodology previously described by considering the dynamic response and the impact on the power plant techno-economic performance. Pelagotti et al. [19] analyzed a header and coil type evaporator for parabolic trough solar plants from the fatigue point of view. A quasi-static stress analysis was used to investigate its response under different ramp rates and varying the value of the header thicknesses to optimize its lifetime. Their results showed that not only the thermal stresses are significant but also the pressure stresses should be carefully considered. A continuation of that work was performed by the authors [20] paying special attention to the two phase flow heat transfer where several correlations were evaluated under different load regimes.

Based on the review presented above, there are no works in the open literature exploring, from a quantitative point of view, the

capabilities of a SG based on the header and coil type design for a STP. In light of the potential benefits such design, as claimed by different references, and the high number issues occurred regarding the reliability of SGs of commercial STPs, it is of interest to explore in a deep manner the capabilities of the novel header and coil design, a concept scarcely studied in the literature. Moreover, it is worth highlighting the added complexity from the structural point of view when the SG is designed for a SPT instead of parabolic trough plants. Such complexity is motivated by the increase of the working temperatures, leading to creep damage besides the fatigue one. Hence, non-trivial phenomena such as creep-fatigue damage combination and stress relaxation are present during operation and should be carefully considered in order to correctly exploit all potential benefits of the header and coil design.

In this work, a design optimization of a header and coil SG for a STP is performed, aiming to minimize the total annual cost, which accounts for the pumping costs and the purchase costs. In addition, several technical constraints have been set in order to obtain suitable designs. Heat transfer and hydraulic models are proposed for the SG design including the critical heat flux calculation in the evaporator. The models have been verified against data reported in the literature for reliable results. Finally, a complete structural assessment of the SG is carried out considering creep-fatigue and stress relaxation phenomena in order to verify the reliability of the promising header and coil SG.

2. Case of study

The CSP plant layout studied, which is shown in Fig. 1, is similar to Crescent Dunes STP [21]. The heat transfer fluid (HTF) is solar salt (i.e., 60% $NaNO_3$ and 40% KNO_3) which is heated in the receiver (R), where solar radiation is concentrated by the heliostat field. The HTF exchanges energy with the water that flows through the exchangers in the SG. Finally, the steam enters the power block to produce electricity. The hot and cold tanks (HT, CT) allow to store the molten-salt in order to keep the heat so it can be used when it is necessary.

The SG consists of four heat exchangers: preheater (PH), evaporator (EV), superheater (SH) and reheater (RH). After expanding in the high-pressure turbine (HP), the steam is reheated in the RH to expand again in the low-pressure turbine (LP). Nominal values of the cycle, restricted by the power block subcritical Rankine cycle, are summarized in Table 1 according to the data from a 110 MWe power block [22]. Additional SG performance parameters are also shown in Table 1. Water and steam properties are calculated using

Table 1
Power block and SG design specifications [22].

| Parameter	Value
High-pressure turbine inlet temperature (°C)	550
High-pressure turbine inlet pressure (bar)	126
Low-pressure turbine inlet temperature (°C)	550
Low-pressure turbine inlet pressure (bar)	34
Feedwater temperature (°C)	245
Salt inlet pressure (bar)	15
Salt inlet mass flow (kg/s)	586
Preheater approach point temperature difference (°C)	10
Evaporator pinch point temperature difference (°C)	2.5
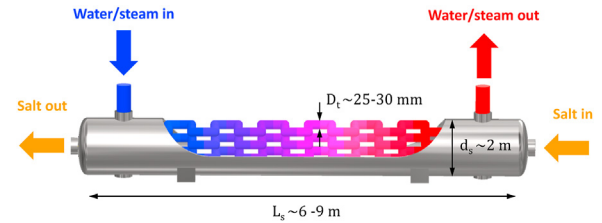
Fig. 2. CAD model of the header and coil heat exchanger.

the correlations shown in Ref. [23]. Molten-salt properties are calculated according to Ref. [24] and are described in detail in Appendix A.

2.1. Geometry

The water and salt flow paths, as well as the heat exchanger geometry are shown in Figs. 2 and 3. The water or steam enters the heat exchanger through the inlet header, flows through the different coils and leaves across the outlet header. On the other hand, the salt flows on the shell side among the tube bundle. If the coils are removed, an approximation of the geometry can be studied as shown in Fig. 3, where N_x and N_y are the number of tube columns and rows, respectively.

The outer diameter of the header can be calculated by distributing every tube of each layer equidistantly around it [15]. Tube and header thicknesses are obtained according to the ASME Section I [16] using Eq. (1). P is the design pressure, D is the outer diameter, S is the maximum allowable stress according to the ASME Code [25], E is the joint efficiency factor, y is the temperature coefficient
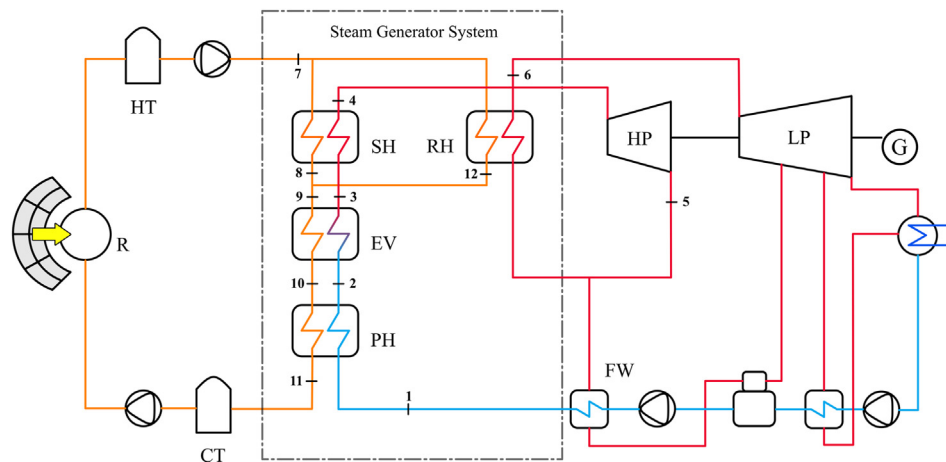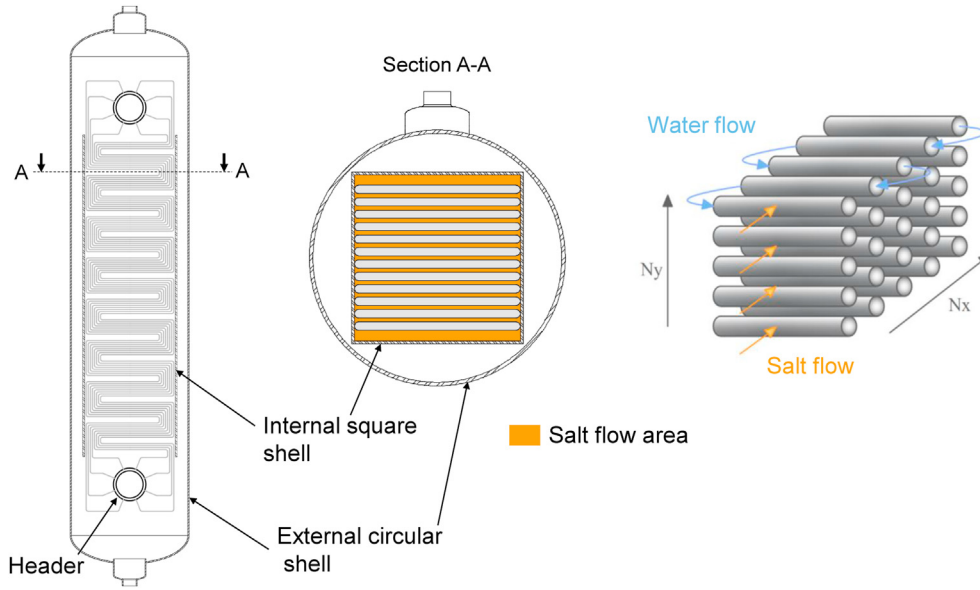

Fig. 1. Solar tower plant layout.

Fig. 3. Header and coil heat exchanger outline and flow path detail.

depending on the material used, and C is the minimum thickness allowance for threading and structural stability.

$$t = \frac{P \cdot D}{2 \cdot S \cdot E + 2 \cdot y \cdot P} + C \tag{1}$$

3. Methodology

3.1. Heat transfer

The heat exchange area, A, is calculated according to Eq. (2). The net heat exchanged, Q, is obtained from the mass and energy balances in all heat exchangers of the SG. ΔT_{lm} is the mean logarithmic temperature difference. F is the temperature correction factor, whose value is fixed to 1 as the heat exchanger is assumed as counter-current. Such hypothesis can be considered as a valid approximation when the number of tube coils is higher than 6 [26].

$$A = \frac{Q}{U \cdot \Delta T_{lm} \cdot F} \tag{2}$$

The overall heat transfer coefficient, U, is determined according to Eq. (3), where R_t and r_t are the outer and inner tube radius, respectively, k is the thermal conductivity of the material tube, and h_t and h_s are the tube and shell heat transfer coefficients, respectively. It is worth noting that fouling resistances have been not considered, following the recommended practice for header and coil SG design [15].

$$\frac{1}{U} = \frac{R_t}{r_t \cdot h_t} + \frac{1}{h_s} + \frac{R_t \cdot \ln\left(R_t/r_t\right)}{k} \tag{3}$$

The heat transfer coefficient on the tube side is determined using the Gnielinski correlation [5]. It is worth mentioning that the tube entrance effects produced by bends have been neglected since the straight tube lengths are typically much larger than 10 times the internal diameter ($L_{t,straight}/d_t \gg 10$) [27]. In the EV, the heat transfer coefficient in the tube side has been corrected to consider two-phase flow effects according to Lockhart and Martinelli correlation [5]. The heat transfer coefficient in the shell side is calculated using Eq. (4), regarded as tube bank in cross flow [28], where j can be obtained using Eqs. (5) and (6), applying the constants a_i that appear in Table 2 as a function of the Reynolds number.

$$h_s = \frac{j \cdot C_P \cdot G_s \cdot \varphi}{Pr_s^{2/3}} \tag{4}$$

$$j = a_1 \left(\frac{1.33}{p_t}\right)^a \cdot \left(Re_{D_t}\right)^{a_2} \tag{5}$$

$$a = \frac{a_3}{1 + 0.14 \cdot \left(Re_{D_t}\right)^{a_4}} \tag{6}$$

The heat flux in the EV should be lower than the critical heat flux to ensure a safe operation. Since the configuration of the EV is horizontal, such critical heat flux is determined according to Wong et al. [29] as shown in Eq. (7). The critical heat flux for vertical orientation is calculated according to Katto and Ohno correlation

Table 2
Constants for convective coefficient and pressure drop of a tube bank in cross flow [28].

Layout angle	Reynolds number	a_1	a_2	a_3	a_4	b_1	b_2	b_3	b_4
90°	$10^5 - 10^4$	0.370	−0.395	1.187	0.370	0.3910	−0.148	6.30	0.378
	$10^4 - 10^3$	0.107	−0.266			0.0815	−0.220		
	$10^3 - 10^2$	0.408	−0.460			6.0900	−0.602		
	$10^2 - 10$	0.900	−0.631			32.1000	−0.963		
	<10	0.970	−0.667			35.0000	−1.000		

P.A. González-Gómez, M. Laporte-Azcué, M. Fernández-Torrijos et al.

Renewable Energy 192 (2022) 456–471

[5]. K_{hor} is the heat flux correction factor, which depends on the water mass flow rate.

$$q''_{crit,hor} = K_{hor} \cdot q''_{crit,ver} \qquad (7)$$

3.2. Pressure drop

The tube side pressure drop is obtained according to Eq. (8), where the first term refers to the friction loss and the second term is due to the direction changes of the flow. f_t is the Darcy friction factor. θ_b and R_b are the bend angle and radius, respectively. K_b is the loss coefficient, which can be determined from Idelchik [30]. ρ_t and u_t are the density and velocity of the water or steam, respectively. The first term must be corrected according to Ref. [5] to take into account the two-phase state appearing in the EV. Contraction and expansion effects at the outlet and inlet of the heat exchangers are also considered as shown in Idelchik [30].

$$\Delta P_t = \frac{1}{2} \cdot f_t \cdot \rho_t \cdot u_t^2 \cdot \left(\frac{\theta_b \cdot R_b + L_t}{d_t} \right) + \frac{1}{2} \cdot K_b \cdot \rho_t \cdot u_t^2 \qquad (8)$$

On the other hand, the shell side pressure drop is calculated according to Eq. (9). The pressure drop for a tube bank in cross flow is calculated according to Taborek [28], where f_s is the friction factor that is estimated according to Eq. (11) and using b_i constants from Table 2. Expansion and contraction effects are again considered when the salt enters and leaves the shell. Moreover, as the header can represent an obstacle in the way of the hot fluid, this can lead to a pressure drop that has been evaluated according to Idelchik [30].

$$\Delta P_s = \Delta P_{s,bank} + \Delta P_{exp/con} + \Delta P_{header} \qquad (9)$$

$$\Delta P_{s,bank} = \frac{2 \cdot f_s \cdot N_x \cdot G_s^2}{\varphi \cdot \rho_s} \qquad (10)$$

$$f_s = b_1 \left(\frac{1.33}{p_t} \right)^b \cdot (Re_{D_t})^{b_2}$$

$$b = \frac{b_3}{1 + 0.14 \cdot (Re_{D_t})^{b_4}} \qquad (11)$$

3.3. Economic analysis

The capital cost of the heat exchangers is estimated using the Purohit method [31] which considers a great number of design parameters. Although this method was developed for conventional shell-and-tube heat exchangers, it has been used to estimate the purchase cost of header and coil heat exchangers in recent studies [15,18]. However, one important differential factor from an economic point of view between conventional and header and coil heat exchangers is the way that the tube joints are welded. While for the conventional exchangers the tube-to-flat tubesheet welds can be made using automatized welding machines, the tube-to-header welds must be made manually. To estimate this extra cost with respect to the conventional shell and tube exchangers, the tube-to-header weld costs have been estimated using data from Ref. [32], which were used to evaluate the cost of a molten-salt central receiver. This extra cost also considers the cost of the nozzle pulled from the header. The welding of the tubes-to-headers require 1.5 man-hours and the nozzles installation demand 2 man-hours. The specific labor cost is estimated to be 85 €/man-hour.

Finally, the capital cost, C_{cap}, is calculated as:

$$C_{cap} = \frac{CE_{index}}{CE_{index,ref}} \left(A \cdot b \cdot \left(1 + \sum_{j=1}^{N_{inputs}} c_j \right) + C_{weld} + C_{nozzle} \right) \qquad (12)$$

where, CE_{index} is the Chemical Engineering Plant Cost Index, c_j is a correction factor for input j (e.g., tube/shell material, pressure work, etc.) and b is the base cost which is calculated as:

$$b = \left(\frac{6.6}{1 - e^{\left(\frac{(7 - d_s)}{27} \right)}} \right) p \cdot f \cdot r \qquad (13)$$

where, d_s is the diameter of the shell, p is the cost multiplier of the tube outer diameter, f and r are cost multipliers of the front and rear head types, respectively.

The material selected for the heat exchangers is the 321H stainless steel which is suitable for molten-salt steam generators [24]. The pumping cost estimation is carried out as shown in Eq. (14). C_e is the electricity cost, which is assumed to be equal to the levelized cost of electricity of the SPT considered in this study. The value of C_e is set to 9.9 c€/kWh which has been estimated using SAM software [33]. H are the plant operation hours which are obtained approximately by means of the capacity factor 62% [33]. It results in 5500 h of operation per year. η is the pump efficiency, considered as 70%.

$$C_{pump}(\text{€}) = C_e \cdot \frac{H}{\eta} \cdot \left(\frac{\dot{m}_t \cdot \Delta P_t}{\rho_t} + \frac{\dot{m}_s \cdot \Delta P_s}{\rho_s} \right) \qquad (14)$$

Once both the capital and pumping costs are estimated, the Total Annualized Cost (TAC) is calculated as shown in Eq. (15), where f_{rc} is the capital return factor obtained considering an 8% interest and 25 years of plant operation.

$$TAC(\text{€}) = f_{rc} \cdot C_{cap}(\text{€}) + C_{pump}(\text{€}) \qquad (15)$$

3.4. Optimization and design constraints

One of the main objectives of this work is to obtain an optimized design of the SG based on header and coil exchangers for a STP. The main design variables selected for such optimization are: i) the number of coils, ii) the shell diameter, and iii) the outer tube diameter. For the evaporator, an additional design variable is considered which is the circulation ratio (or the outlet steam quality). Four discrete values are selected for the outer tube diameters: 25 mm, 30 mm, 38 mm and 50 mm, which are typically used in the industry [34]. The upper and lower bound values of these variables are shown in Table 3.

Additionally, different technical constraints based on good practices have been regarded in order to obtain feasible designs and to reduce computational effort as well:

- The minimum velocities on shell-and-tube sides are set to 0.2 m/s and 0.5 m/s to avoid excessive fouling rates [3].

Table 3
Optimization design variables.

Parameter (Units)	Lower bound	Upper bound
Tube outer diameter index (−)	1	4
Circular shell diameter, d_s (m)	0.8	2.5
Number of tube coils (−)	10	50
Evaporator circulation ratio (−)	2	15

- The maximum shell side velocity is set to 1.5 m/s to prevent tube vibration problems.
- The maximum tube side velocity is limited to avoid excessive erosion, vibrations and/or noisy problems. For water it is set to 4 m/s [35] and for steam is calculated as: $u_{t,max} = 175(1/\rho_t)^{0.43}$ [36].
- The maximum circular shell diameter is set to 2.5 m [34].
- A tube pitch ratio equal to 1.25 has been selected since this value yields the highest heat transfer coefficients [15].
- The maximum pressure drop on the steam side in the RH is limited to 1 bar in order to meet LP turbine inlet constraints.

The objective of the optimization is to minimize the TAC, which accounts for the annualized heat exchangers capital cost and pumping costs on shell/tube sides. Due to the relatively low number of design variables compared to shell-and-tube exchangers, the optimization algorithm can be simplified, being feasible to sweep all the domain considering all the possible variable combinations.

3.5. Thermo-mechanical analysis

In thermal power plants, creep, fatigue, or creep-fatigue damages should be considered in the design phase of their thermal equipment since these are potential failure mechanisms. Creep damage appears when working under nominal conditions and high temperatures, when the stress levels are almost constant. Due to the high temperatures experienced by the SG, creep damage must be considered. Fatigue damage appears when transient events such as start-up, shutdown or load changes take place. Creep-fatigue interaction must be regarded as well as it may lead to an accelerated damage, reducing the expected lifetime.

In previous studies focused on header and coil heat exchangers, the tube and header joint was identified as the most critical point of failure [15,19]. Fig. 4 shows the tube and header joint (point P) that will be analyzed in detail here.

3.5.1. Stress analysis

The total elastic stress, σ^E, in the tube and header joint is calculated by means of Eq. (16), which considers the thermal elastic stress, σ_T^E, and the mechanical elastic stress, σ_M^E, which are determined according to the European standard EN 12952-3 [17]. Thermal and mechanical concentration factors, α_T and α_M, respectively, have to be applied to correctly estimate the stress. The thermal stress, Eq. (17), depends on the thermal expansion coefficient β, the Young's modulus E, the Poisson's ratio v, the mean wall temperature T_m and the inner wall temperature $T_{r=r_{head}}$. For these two last parameters, the header wall temperature profile can be deduced according to the heat diffusion equation restricted only in

the radial direction, where the initial and boundary conditions are shown in Eq. (18). α and k are the thermal diffusivity and thermal conductivity, respectively. The internal heat transfer coefficient h_i, is calculated using the Gnielinski correlation [5]. The outer coefficient h_o, is deducted according to the Hilpert correlation [37]. This equation is solved using the Crank-Nicolson method [38].

$$\sigma^E = \alpha_M \cdot \sigma_M^E + \alpha_T \cdot \sigma_T^E \tag{16}$$

$$\sigma_T^E = \frac{\beta \cdot E}{1 - v} \cdot (T_m - T_{r=r_{head}}) \tag{17}$$

$$\begin{cases} \dfrac{1}{\alpha} \dfrac{\partial T}{\partial t} = \dfrac{1}{r} \dfrac{\partial}{\partial r} \left(r \dfrac{\partial T}{\partial r} \right) \\ T(r,0) = T_0 \\ -k \dfrac{\partial T}{\partial r} \Big|_{r=r_{head}} = h_i \cdot (T_i - T(r_{head}, t)) \\ -k \dfrac{\partial T}{\partial r} \Big|_{r=R_{head}} = h_o \cdot (T(R_{head}, t) - T_o) \end{cases} \tag{18}$$

The mechanical stress can be deducted from Eq. (19), where P is the internal pressure. $D_{m,head}$ and t_{head} are the header average diameter and thickness, respectively.

$$\sigma_M^E = P \cdot \frac{D_{m,head}}{2 \cdot t_{head}} \tag{19}$$

3.5.2. Fatigue damage

The fatigue damage is estimated according to European standard EN 12952-3 [17]. The corrected stress range, $2\sigma_{fa}$, is determined as:

$$2\sigma_{fa} = \frac{\Delta\sigma^E C_k C_P}{C_{T*}} \tag{20}$$

where the notch factor is set to $C_k = 1.3$, selected according to typical values for fatigue assessment of tube and header connections [39], C_{T*} and C_P are temperature and plasticity correction factors calculated according to EN 12952-3 [17]. The number of allowable cycles, N_A, is determined through Eq. (21), where R_m is the ultimate tensile strength of the material. Firstly, N_A^* is determined using a correction factor on the stress range as $2\sigma_{fa,s} = 1.5 \cdot 2\sigma_{fa}$. Secondly, N_A^{**} is determined using a correction factor of 10 on the allowable number of cycles. Then, the number of allowable cycles for a given stress range is calculated as $N_A = \min(N_A^*, N_A^{**})$. It is worth noting that these factors are not actually factors of safety; rather, they are intended to adjust small, polished test specimen data to make it applicable to actual components [40].

$$2\sigma_{fa} = 0.8 \cdot R_m + (173150 - 0.8 \cdot R_m) \cdot N_A^{-0.547} \tag{21}$$

Finally, the fatigue damage D_f is calculated according to Eq. (22) assuming 300 startups per year, resulting in a total number of cycles: $M = 300 \cdot n_{year}$.

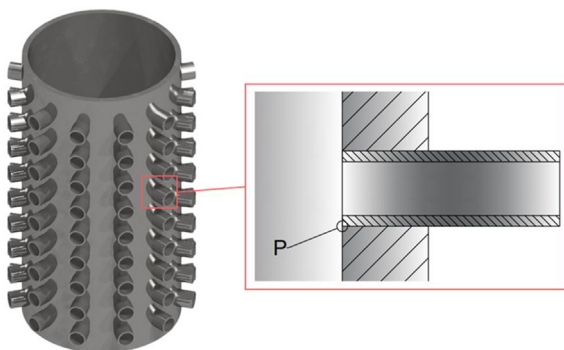$$D_f = \sum_{j=1}^{M} \frac{N_j}{N_{A,j}} \tag{22}$$

Fig. 4. Tube-to-header joint: critical point (P) and tube distribution.

P.A. González-Gómez, M. Laporte-Azcué, M. Fernández-Torrijos et al.

Renewable Energy 192 (2022) 456—471

Table 4
Stress-strain curve data for 321H stainless steel from Ref. [42].

Material	Temperature (°C)	Monotonic stress/strain curve		Cyclic stress/strain curve	
		K (MPa)	n (−)	K' (MPa)	n' (−)
321H stainless steel	540	385.7	0.189	1928	0.361
	20	460.6	0.138	2082	0.317

3.5.3. Creep damage

Due to the high stress levels experienced in the tube-to-header joints, permanent plastic deformations are expected to appear. Such conditions should be considered for a proper estimation of the creep damage. The elastic-plastic stress, σ, can be deducted according to the Neuber's equation shown in Eq. (23):

$$\sigma^E \cdot \varepsilon^E = \frac{\sigma^2}{E} + \sigma \cdot \left(\frac{\sigma}{K}\right)^{1/n} - \sigma \cdot \varepsilon_{offset} \tag{23}$$

where ε_{offset} is calculated according to Kalnins [41]. K and n are experimental parameters whose values are summarized in Table 4, which have been obtained by fitting from the experimental data available in Ref. [42]. If the stress is greater than twice the elastic limit, the cyclic stress-strain curve should be used. If not, monotonic curves are better suited instead.

An important effect to avoid creep damage overestimation is the stress relaxation, whose consideration is highly recommended for accurate lifetime predictions [43]. The stress relaxation is a time dependent phenomenon where loading equipment exposed to high temperature experience a stress decrease. This effect is due to the conversion of elastic strain into inelastic strain during the dwell period under constant strain conditions [44]. A simplified method with a reasonable accuracy to estimate the stress relaxation consist of using isochronous stress/strain curves. In ASME Section III Subsection NH [9], it can be found a complete set of guidelines about its use to calculate time dependent structural problems like cyclic creep deformations and local creep relaxation at stress concentrations for creep/fatigue evaluation [45].

The creep strain rate of 321H stainless steel has been modeled using Monkman-Grant model as [46]:

$$\dot{\varepsilon}_c = \frac{c_{MG}}{10^{\frac{c_1 + c_2 \, \log(\sigma) + c_3 \, \log(\sigma)^2}{T - 273.2}} - c_0} \tag{24}$$

where $\dot{\varepsilon}_c$ is the minimum creep strain rate expressed in 1/hours, T is the temperature expressed in Celsius and σ is the stress expressed in MPa. The rest of parameters are constants whose values are summarized in Table 5.

Once the elastic-plastic and creep strain/stress models of the material are defined, the isochronous curve can be built. Fig. 5 shows the isochronous curve of 321H stainless steel at 550 °C and times of exposures between 0 and $2 \cdot 10^5$ h.

It should be noted that the stress relaxation experienced by high temperature equipment is dependent on the loading conditions, where the two extreme cases are: stress resetting where each cycle begins the relaxation at the same stress value, or global stress relaxation where the equipment experiences a single relaxation

Table 5
Constants values for creep strain rate model of stainless steel 321H [46].

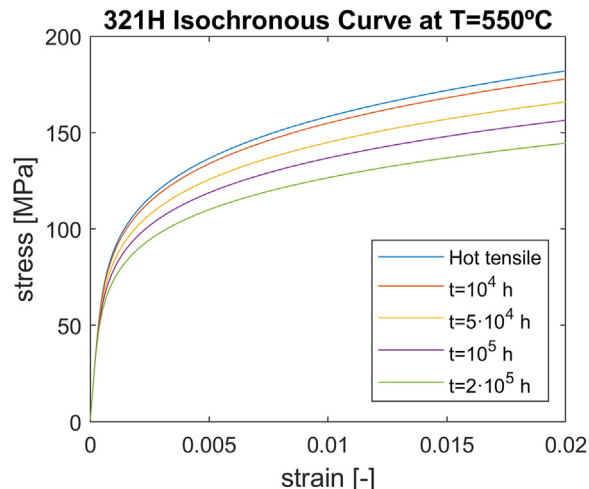| Constant values	c_0	c_1	c_2	c_3	c_{MG}
	12.70	1470	7885	−768	0.009

Fig. 5. Isochronous curve of 321H stainless steel at 550 °C.

curve non-restarted in between start-up/shutdown cycles [47]. The last one is a desirable working condition because the creep damage is significantly reduced due to the low stress levels. Therefore, it is critical to determine the loading conditions for which a structure follows global stress relaxation. According to Becht [48] stress resetting will not occur if the elastically calculated stress range is less than the cold yield strength ($S_{y,c}$) plus the hot relaxation strength (S_H), i.e. $\Delta\sigma^E < S_{y,c} + S_H$, where S_H is estimated as 1.25 times the ASME allowable stress S evaluated at dwell temperature [48].

Finally, the creep damage, D_c, is obtained according to Eq. (25). Considering 5500 h of operation per year, the dwell period is calculated as: $H = 5500 \cdot n_{year}$.

$$D_c = \int_0^H \frac{dt}{t_R\left(\sigma_{eff}^{creep}, T\right)} \tag{25}$$

The time to rupture of 321H stainless steel is obtained from the datasheets provided by the European Creep Collaborative Committee [49]. The effective creep stress is calculated applying a security factor as: $\sigma_{eff}^{creep} = \sigma^{relax}/K_{safe}$. A value of $K_{safe} = 0.9$ is chosen according to Refs. [50,51] instead of 0.6 used by nuclear plant code ASME Section III Subsection NH [9]. Structural failures in CSP plant have significant lower level of risk than nuclear plants. Besides, higher security factors may lead to ineffective cost increase. On the other hand, stress relaxation limit should be considered due to the high working pressure of the steam generator exchangers. This limit is determined in two steps: i) the normalized pressure stress ($X = \sigma_M^E/S_y$) and the normalized thermal stress ($Y = \sigma_T^E/S_y$) are calculated; ii) these values are used to calculate the normalized lower bound stress $Z = \sigma_{LB}/S_{y,c}$ according Figure HBB-T-1332-1 of ASME Section III Subsection NH [9], where the creep effective stress considering stress relaxation has to satisfy: $\sigma_{eff}^{creep} \geq \sigma_{LB}$.

3.5.4. Lifetime calculation. Creep-Fatigue interaction

According to the ASME Code, the total damage produced by the interaction of fatigue and creep is calculated by summing up each individual damage, as shown in Eq. (26). Following the approach employed in Ref. [42], the damage limit, D_L, of 321H stainless steel is set as the 304 and 316 stainless steels creep-fatigue damage interaction rule according to ASME Section III Subsection NH [9].
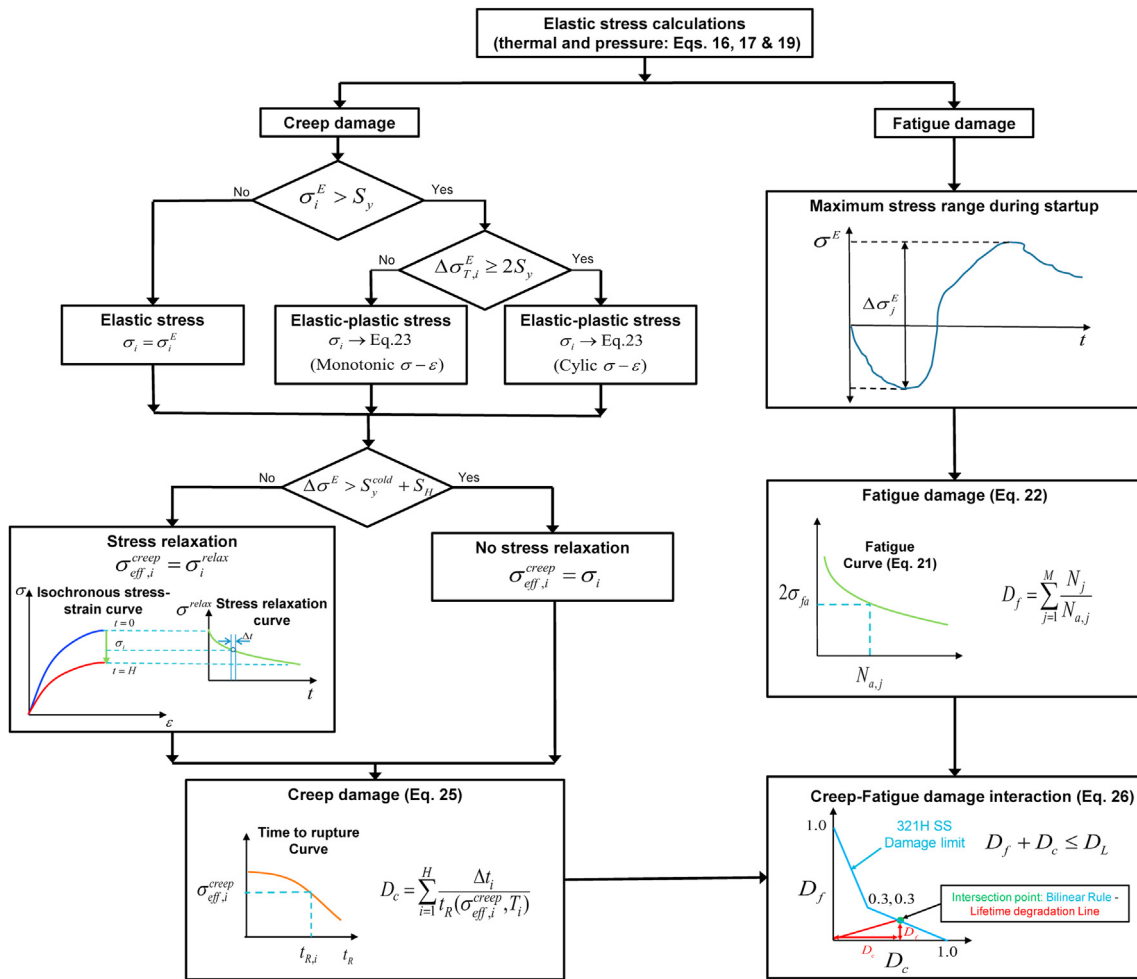
Fig. 6. Schematic of the lifetime calculation procedure considering creep-fatigue damage interaction.

Table 6
Verification results.

Parameter (Units)	SH results model	SH results [15]	Deviation SH (%)	Deviation PH (%)
Tube side velocity (m/s)	6.396	6.5	−1.5914	−3.277
Shell side velocity (m/s)	1.043	1.01	3.3609	0.058
Tube side pressure drop (bar)	0.403	0.472	−14.436	3.400
Shell side pressure drop (bar)	0.423	0.445	−4.8323	1.543
Tube side heat transfer coefficient (W/m²K)	1929.32	2024.3	−4.6919	−1.220
Shell side heat transfer coefficient (W/m²K)	2062.46	1866.1	10.522	7.749
Shell length (m)	15.67	15.0300	4.2910	2.150
Header diameter (m)	0.4696	0.4659	0.7943	1.698

$$D_f + D_c \leq D_L \tag{26}$$

Lastly, the lifetime of the heat exchangers, n_{year}, is calculated by an iterative process until the total damage, $D_f + D_c$, converges into the damage limit D_L. A schematic of the lifetime calculation procedure is depicted in Fig. 6.

4. Results and discussion

4.1. Model verification

Table 6 shows the comparison between the results obtained following the presented methodology for mechanical design, heat transfer and pressure drop calculations, and the results of header and coil heat exchangers available in the literature [15]. It should be noted that the results presented in Ref. [15] are referred to a 55 MWe parabolic through power plant using Therminol-VP1 as HTF. Hence, reasonable deviations are observed in the main design parameters such as velocities, header diameters, exchanger lengths, pressure drops and heat transfer coefficients. In light of the results, it can be concluded that the presented methodology yields predictions with a reasonable level of accuracy.

4.2. Optimization results

Fig. 7 shows every solution that satisfies the imposed constraints for each heat exchanger of the SG. Both water and HTF
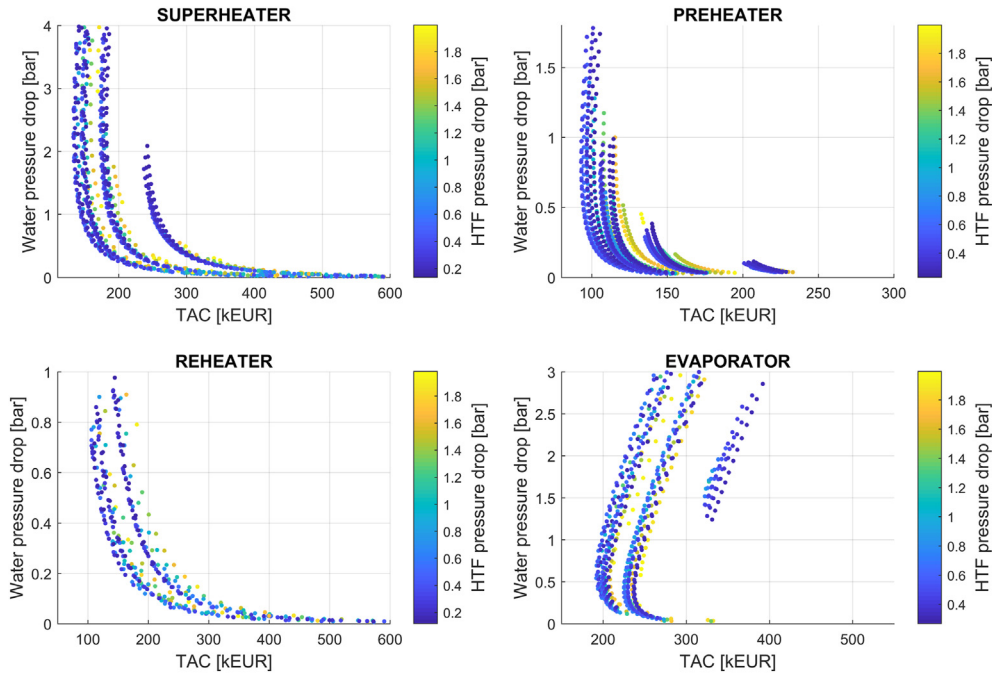
P.A. González-Gómez, M. Laporte-Azcué, M. Fernández-Torrijos et al.

Renewable Energy 192 (2022) 456–471

Fig. 7. Optimization results. Pressure drop vs TAC.

pressure drops are plotted against the TAC. As it can be seen, different trade-offs are obtained for the SH, PH and EV, which are generated by each tube size analyzed. In contrast, the RH does not show a trade-off for TAC. This is mainly due to the fact that the pumping cost on the water side is not being considered in TAC since the RH is downstream of the HP turbine inlet and therefore the high-pressure pump of the power block does not provide extra pressure due to the pressure drop in the RH. Then, the increase of the pressure drop leads to a decrease of the heat transfer area and lower capital cost for RH. Effectively so, the higher the velocity of the steam, the higher the pressure drop and the heat transfer co-efficient. The heat transfer coefficient on the steam side dominates over the overall heat transfer coefficient in the SH and RH, while the heat transfer coefficient on the shell side dominates in the EV and PH. For this reason, the optimum values are obtained for high pressure drops on the water side for SH and RH, and optimum

values are obtained for low pressure drops on water side for EV and PH.

In order to analyze the solutions presented in Fig. 7, Table 7 shows the detailed outcome for the lowest TAC solution. The RH obtains the lowest TAC value as a result of neglecting the pumping cost on the water side. On the other hand, the EV shows the highest TAC due to the large heat transfer area and pumping costs of both fluids. Note that a forced circulation EV is employed in this work, increasing significantly the pumping costs compared to a natural circulation EV.

The optimum solution that minimizes TAC for the header and coil SG yields a total pressure drop on the shell and tube sides of 1.4 and 2.2, respectively. Note that the SH has been omitted for the shell side pressure drop calculation since it is in parallel with the RH. The RH is omitted on the tube side pressure drop calculation since it does not yield pumping cost. The total purchase cost is

Table 7
Lowest TAC solution results.

Parameter (Units)	Superheater	Reheater	Evaporator	Preheater
Shell diameter (m)	2	2.1	2	2.1
Tube diameter (mm)	25	30	25	25
Tube thickness (mm)	3.3	2.0	2.6	2.5
Shell length (m)	7.7	6.9	9.0	5.6
Number of tube coils (−)	23	13	13	39
Header diameter (m)	0.404	0.522	0.588	0.180
Cold header thickness (mm)	21.2	8.4	28.9	8.7
Hot header thickness (mm)	32.5	12.7	31.2	8.8
Water/Steam average velocity (m/s)	14.96	23.75	1.77	1.70
HTF average velocity (m/s)	0.48	0.28	0.77	0.67
Tube side pressure drop (bar)	2.232	0.697	0.693	0.823
Shell side pressure drop (bar)	0.292	0.163	0.695	0.419
Tube side heat transfer coefficient (W/m²K)	3312.5	1150.0	32948.0	13013.4
Shell side heat transfer coefficient (W/m²K)	4407.9	3049.0	5331.5	4269.0
Overall heat transfer coefficient (W/m²K)	1232.2	697.8	2703.9	2078.5
TAC (k€)	133.1	107.2	192.1	93.0
Purchase cost (k€)	1123	1126	1555	792

4.5 M€ without considering piping, valves, sensors, etc.

The optimum designs are obtained for the outer tube diameter of 25 mm in all exchangers, except for the RH, whose optimum value for the outer tube diameter is 30 mm. The optimum designs aim towards small tube diameters because they have the smallest cost multiplier due to the tube diameter (*p*) according to Purohit method, and also provide the lowest tube thickness compared to the other size options. Additionally, small tube diameters present the advantage of maximizing the heat transfer area for a fixed heat exchanger volume.

From the heat transfer point of view, the main advantage of the header and coil SG is that it provides a higher convective coefficient on the shell side for the same velocity compared to a conventional shell-and-tube SG. The effective cross flow provides economically-effective heat transfer coefficients with low pressure drops on the shell side, which lead to significant savings in the pumping costs. For example, using the data provided in section 3.3, the shell side pumping cost for the header and coil SG is around 37 k€/year, while for the shell-and-tube SG is around 136 k€/year (the pressure drop on the shell-and-tube SG for 100 MWe STP was obtained from Ref. [4]).

The results of the critical heat flux analysis for the EV are shown in Fig. 8. The optimum circulation ratio is 4 which means a maximum allowed steam quality of 25% at the EV outlet. The design proposed for the EV can be considered safe since the actual heat flux is below of the critical heat flux along the EV length.

4.3. Thermo-mechanical results

Fig. 9 illustrates the hot (daily) startup of the steam generator which has been modeled considering constraints of a typical 100 MWe steam turbine used in solar thermal power plants. This is an adaption of what is shown in Ref. [2]. The main thermodynamic variables are used as inputs for the heat transfer and stress analysis in the tube-to-header joints. The startup is completed in 45 min. The initial salt and steam temperatures are 290 °C. The inlet salt temperature raises until it reaches 565 °C while the steam outlet temperature stops at 550 °C. The initial SH steam outlet pressure is 74 bar and rises until 126 bar. The steam mass flow evolves from around 20 kg/s to 86 kg/s. The salt mass flow goes from 100 kg/s to over 586 kg/s. The start-up curve has an average temperature change rate of 6.1 K/min. However, the relevant stresses should appear during the first 10 min, where there is a temperature change rate of 20 K/min. It is worth mentioning that the SH efficiency
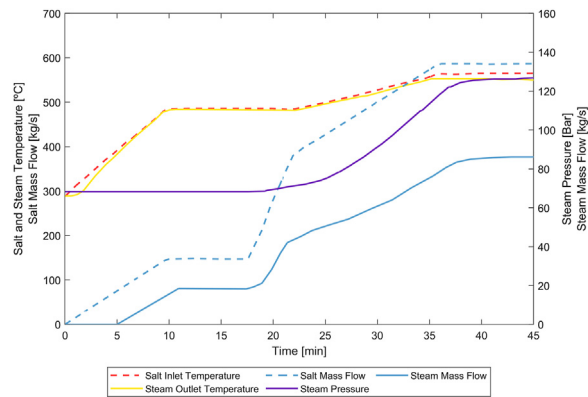

Fig. 9. Temperature, pressure and mass flow inputs for the stress analysis.

varies during the startup, where at some instants, it is near to 0.99 and therefore the steam outlet temperature is very close to the salt inlet temperature.

Fig. 10 shows the total stress evolution as well as its thermal and pressure components in the SH. As it can be seen, the pressure stresses evolve in the same way as the steam pressure shown in Fig. 9, which present their maximum value when the nominal conditions are achieved. Contrary to the pressure stresses, the thermal stresses achieve their maximum values during the transient operation, where the temperature difference between outer and inner header walls is maximum.

Table 8 summarizes the stress and creep-fatigue results of the SG together with the lifetime predictions. The most critical point is obtained in the EV hot header, with an extraordinary low lifetime prediction of 2.4 years and being fatigue the main mechanism of failure. The lifetime estimation for the SH and RH hot headers are 14.3 and 12.9, respectively, which are below the typical lifetime design targets of 25 or 30 years. The main mechanism of damage is creep in both cases due to the high working temperatures (~550 °C) and the pressure stress concentrations around the tube-to-header connection. Lastly, the SH cold header obtained a lifetime of 11.6 years, again below the minimum design targets. In this case, the main damage mechanism is fatigue due to the large stress ranges obtained from the combination of pressure and thermal stresses (see Fig. 10). Similar to the EV hot header, the source of the high thermal stress is obtained due to the high temperature difference between the outer and the inner walls (ΔT ~120 °C).

In light of the poor results obtained in the creep-fatigue analysis of the SG, different redesign actions are investigated in order to improve the lifetime of aforementioned critical points. Fig. 11 shows the evolution of the SH lifetime when the thickness is increased. In the hot header (Fig. 11 a), where the steam gets out and the salt comes in, the lifetime increases to a maximum of 27 years (red line) as the thickness goes up. The sudden drop of the lifetime is due to the stress reset limit being surpassed, and therefore, after that, the stress relaxation effect is not considered (blue line). However, the lifetime continues to increase as the thickness does so due to the decrease of the pressure stress, which reduces the creep damage. It is worth mentioning that the method of ASME Section I [16] seems not to be suitable for a final thickness sizing due to the low lifetime obtained for the SH hot header. Although creep is the dominant damage mechanism at the SH hot header, and the ASME *S* allowable stress limit considers more than 10^5 h of exposure to a creep damage at the corresponding working temperature [52], the design that results from the simplified methodology of ASME Section I [16] cannot be considered as a definitive one because it does not take into account the stress
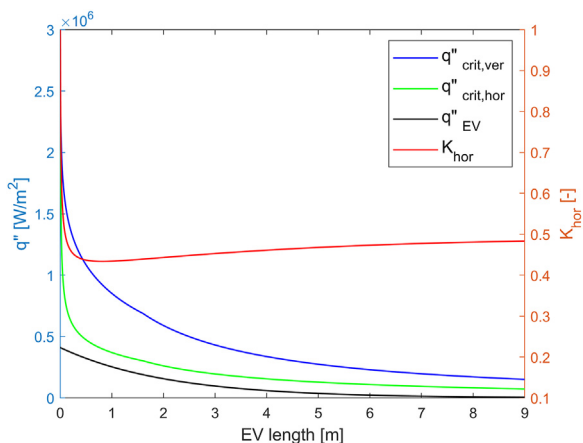

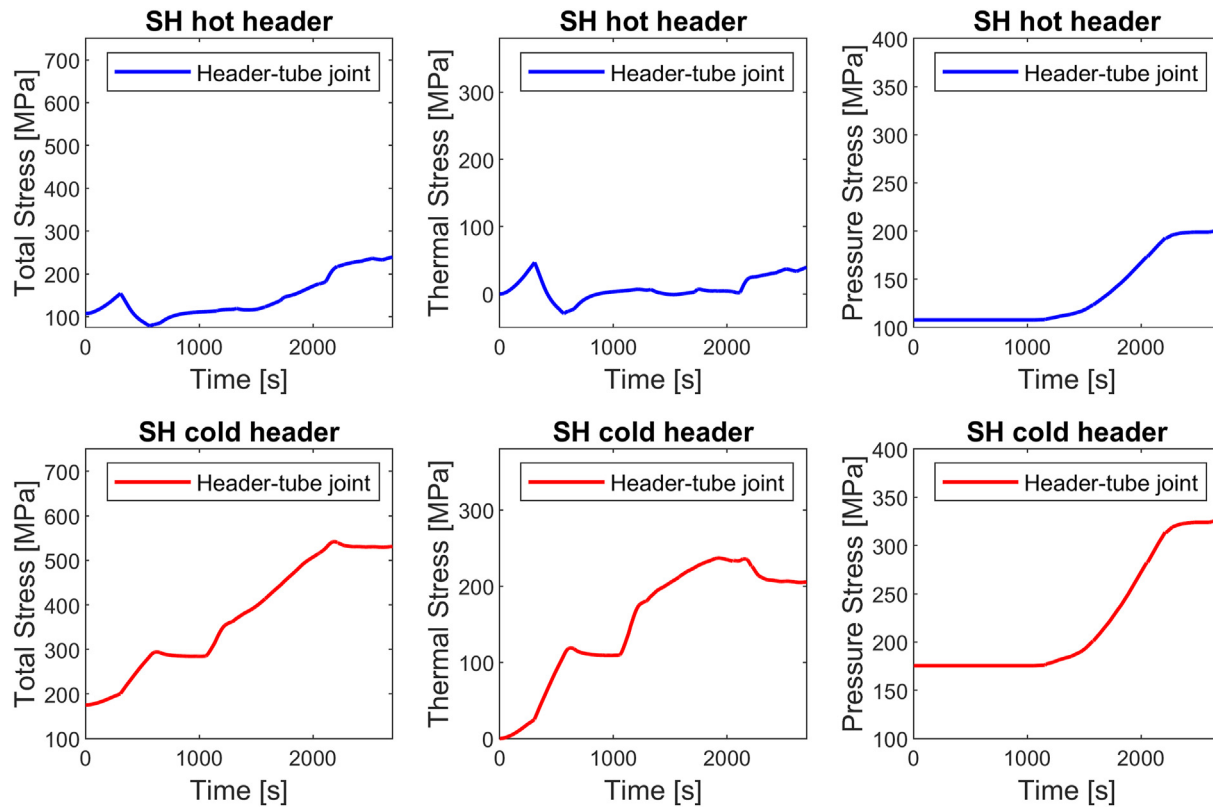**Fig. 8.** Critical heat flux check results.

Fig. 10. Total (left), thermal (centre) and pressure (right) stress at the hot (first row) and cold (second row) headers of the SH.

Table 8
Stress and creep-fatigue results.

Point	Parameter (Units)	SH	RH	EV	PH
hot header	Max. elastic stress range, $\Delta\sigma^E$ (MPa)	209.1	156.1	649.8	262.7
	Max elastic stress, σ^E (MPa)	237.5	239.7	645.2	433.1
	Total creep damage, D_c	0.992	0.994	0	0
	Total fatigue damage, D_f	0.004	0.003	1	1
	Lifetime, n_{year} (years)	14.3	12.9	2.4	>1000
cold header	Max. elastic stress range, $\Delta\sigma^E$ (MPa)	476.7	235.5	203.9	340.1
	Max elastic stress, σ^E (MPa)	531.2	363.9	331.1	494.6
	Total creep damage, D_c	0	0	0	0
	Total fatigue damage, D_f	1	1	1	1
	Lifetime, n_{year} (years)	11.6	>1000	>1000	390

concentrations due thermal and pressure loads occurred in the tube-to-header connection.

On the other hand, in the cold header of the SH (Fig. 11 b), where there is no creep damage, once the thickness starts to increase the pressure stresses are reduced until reaching a maximum lifetime of 12.7 years. Beyond this point, the lifetime decreases because the drop of the pressure stresses does not balance the growth of the thermal stresses. If the thickness continues to increase, the thermal stress is more harmful and thus the SH lifetime is gradually reduced. Again, the analytical design method proposed by ASME Section I [16] for header sizing fails, now due to the ASME method does not consider fatigue damage.

Fig. 12 illustrates the lifetime evolution of RH hot header when the thickness is increased. Additionally, the lifetime evolution without considering the stress relaxation is also plotted. As it can be seen, suitable lifetimes are obtained above of 25 mm if the stress relaxation is considered. If not, the valid thicknesses are obtained above of 32 mm, approximately. Despite the damage in the hot

header of RH is dominated by creep, the ASME Section I [16] method is not suitable for a final design due to the reasons aforementioned for the SH hot header case.

As shown earlier, in those points where fatigue is the dominant damage mechanism, the increase of the header thickness is not effective to increase the lifetime (see Fig. 11 b). In order to meet the minimum design lifetime target of 25 years, different redesign actions have been explored. For example, one possible redesign action to increase the lifetime consists in reducing the heat transfer coefficient on the outer wall of the header. This reduces the temperature difference between the inner and the outer header wall and, consequently, it reduces the thermal stress and the fatigue damage. Figs. 13 and 14 depict the evolution of the lifetime for the cold SH and hot EV headers when the salt velocity is varied. As it can be seen, the results show that this redesign action results effective for the lifetime increase, since the velocity levels for suitable lifetimes seem reasonable. Specifically, for a 30-year lifetime, velocities of 0.27 m/s and 0.12 m/s must be obtained around
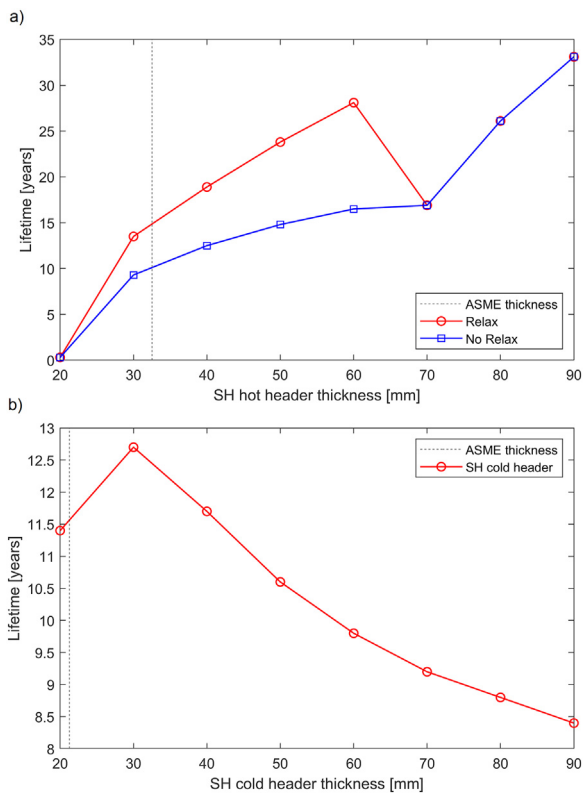
P.A. González-Gómez, M. Laporte-Azcué, M. Fernández-Torrijos et al.

Renewable Energy 192 (2022) 456–471

a)

b)

Fig. 11. Lifetime vs SH headers thickness: a) hot and b) cold.

Fig. 12. Lifetime vs thickness of the hot header of the RH.

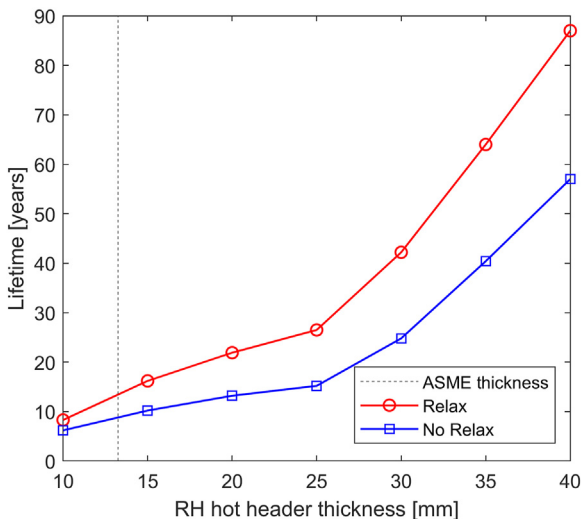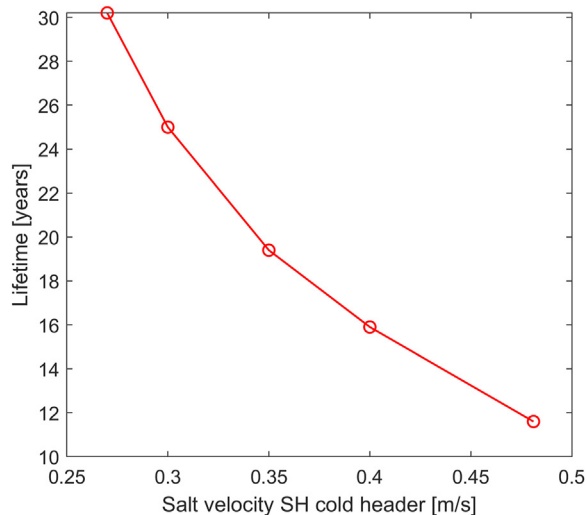**Fig. 13.** Lifetime vs salt velocity at the cold header of the SH.
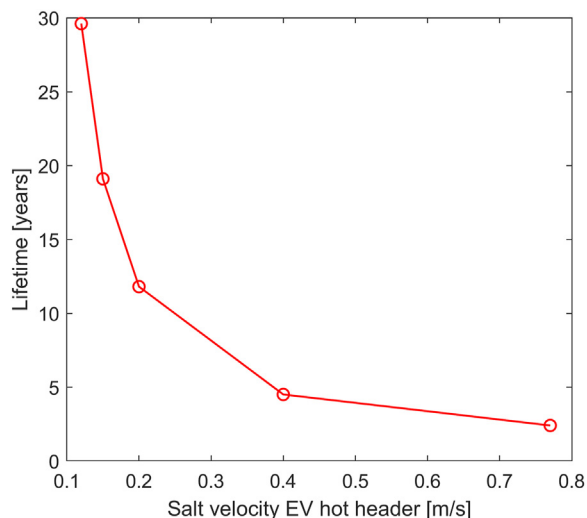
Fig. 14. Lifetime vs salt velocity at the hot header of the EV.

SH cold and EV hot headers, respectively. The external heat transfer coefficients are reduced from 1205.6 W/m²K to 734.15 W/m²K for the SH cold header, and from 1643.2 W/m²K to 367.9 W/m²K for the EV hot header.

The salt velocity impacting on the external header surface can be reduced if the hydraulic resistance is increased around the header. When the shell side fluid leaves the internal square shell, two flow paths are generated, one flowing through the tube bank and header (path 1), and other flowing through the area between

the circular shell and the tube bank, i.e. the tube-bundle to shell clearance (path 2) (see Fig. 15). Bearing in mind that the hydraulic resistance of the flow 1 is higher than the flow path 2, and that the pressure drops at the salt outlet nozzle must be the same for both flow paths, an important amount of mass flow rate is by-passed through the second path, reducing in this way the actual salt velocity around the header. In order to estimate the mass flow rates of each path, the Stream Analysis Method [5] is employed. The final results are summarized in Table 9. The estimated velocities around the SH cold and EV hot header are below the maximum allowed, indicating that both designs can be considered now in the safety side. It is worth noting that only four tube rows have been assumed before the flow 1 impacts on the header. However, to increase the margin of safety, the number of tube rows can be increased (and the hydraulic resistance of the flow 1), decreasing even more the velocity around the header as a result.

5. Conclusions
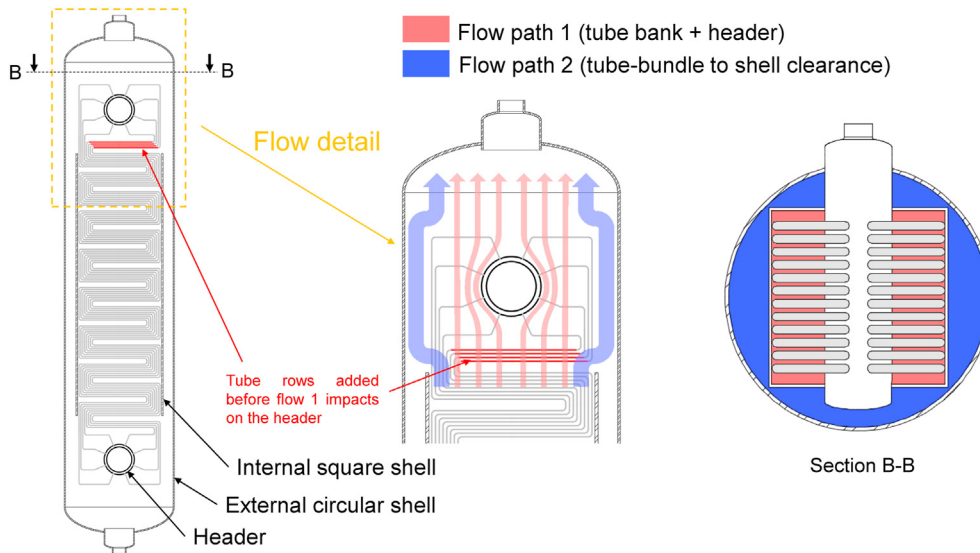
A complete methodology was presented for the design and

P.A. González-Gómez, M. Laporte-Azcué, M. Fernández-Torrijos et al.

Renewable Energy 192 (2022) 456—471

Fig. 15. Schematic of the flow paths around the header.

Table 9
Hydraulic results of the shell side flow paths around headers.

Point	Parameter (Units)	Value
SH cold header	Maximum allowed velocity around header (m/s)	0.270
	Actual velocity around header (m/s)	0.066
	Salt mass flow through path 1 (%)	13.7
	Salt mass flow through path 2 (%)	86.3
	Number of tube rows before the flow 1 impacts on the header	4
EV hot header	Maximum allowed velocity around header (m/s)	0.120
	Actual velocity around header (m/s)	0.098
	Salt mass flow through path 1 (%)	12.6
	Salt mass flow through path 2 (%)	87.4
	Number of tube rows before the flow 1 impacts on the header	4

optimization of the header and coil steam generator for a solar tower plant, aiming to minimize the total annual cost, considering the pumping costs and the exchangers capital costs. Several technical constraints were set in order to obtain proper designs. Heat transfer and hydraulic models were proposed for the steam generator sizing including critical heat flux calculation in the evaporator. These models have been verified against other header and coil exchangers designs reported in the literature, obtaining suitable accuracy levels. Finally, a methodology for the structural assessment was addressed considering creep-fatigue and stress relaxation phenomena in order to verify the structural capabilities of the header and coil steam generator.

Based on the results showed above, the following conclusions are obtained:

• The optimum solution that balances the total capital and pumping cost for the header and coil steam generator obtains a total pressure drop on the shell and the tube sides of 1.4 and 2.2, respectively. The purchase cost is 4.5 M€ considering only the heat exchangers.
• One important advantage of the header and coil steam generators is that they provide more economically effective overall heat transfer coefficients with lower pressure drops on the shell

side than conventional shell-and-tube steam generators. From a quantitative point view, the annual pumping costs in the shell side are reduced by around 3.6 times.
• The critical spots from the creep damage point of view were the superheater and reheater hot headers, whose thickness calculation using ASME Section I [16] yields lifetimes much lower than typical design targets.
• The structural assessment of the steam generator reveals that ASME Section I [16] method is not suitable for the final sizing of the header thickness. This is mainly because it does not consider the stress concentrations due to thermal and pressure loads that occur in the tube-to-header connections.
• From the fatigue point of view, the critical areas are the superheater cold and evaporator hot headers, which exhibit high stresses due to large temperature differences between the outer and inner header walls. The heat transfer coefficients at the outer wall of the headers have a strong influence in the lifetime at the aforementioned spots, showing the importance of keeping the salt velocities around headers in suitable levels.
• The increase of the hydraulic resistance around the header is an effective practice to reduce the velocity and the heat transfer coefficient on the external header surface. As the hydraulic resistance around the header increases, the secondary flow

through tube-bundle to shell clearance captures a greater amount of the total mass flow rate of the shell side. In this way, a reduction of the mass flow and the velocity of the primary flow path impacting on the header surface is obtained.

- The results showed that the header and coil steam generator is able to operate with fast daily startups at 6.1 K/min without having its structural integrity compromised. Compared to a steam generator based on conventional shell-and-tube exchangers, that implies a significant improvement on the temperature rate change, specifically 2.4 times higher, leading to a consequent startup time reduction for a daily startup.
- To conclude, if a solar tower plant was to be operated as a load-following plant, the header and coil steam generator would be one potential solution to provide high flexibility without increasing the forced outages. Despite the higher purchase cost compared to the conventional shell-and-tubes steam generator, the potential revenue increase coming from the participation in grid balancing services could balance the higher initial cost.

CRediT authorship contribution statement

M. Laporte-Azcué: Conceptualization, Methodology, Software, Writing − review & editing. **M. Fernández-Torrijos:** Conceptualization, Methodology, Software, Writing − review & editing. **D. Santana:** Resources, Conceptualization, Writing − review & editing, Supervision, Funding acquisition.

Declaration of competing interest

The authors declare that they have no known competing financial interests or personal relationships that could have appeared to influence the work reported in this paper.

Acknowledgements

Appendix A. Molten-salt properties

References

[1] P. del Río, C. Peñasco, P. Mir-Artigues, An overview of drivers and barriers to concentrated solar power in the European Union, Renew. Sustain. Energy Rev. 81 (2018) 1019—1029, https://doi.org/10.1016/j.rser.2017.06.038.
[2] I. Agnetti, Highly reliable steam generator system developed by John Cockerill Energy for peaker plants, AIP Conf. Proc. 2303 (2020), https://doi.org/10.1063/5.0028683, 0—9.
[3] P.A. González-Gómez, F. Petrakopoulou, J.V. Briongos, D. Santana, Cost-based design optimization of the heat exchangers in a parabolic trough power plant, Energy 123 (2017) 314—325, https://doi.org/10.1016/j.energy.2017.02.002.
[4] P.A. González-Gómez, J. Gómez-Hernández, J.V. Briongos, D. Santana, Thermo-economic optimization of molten salt steam generators, Energy Convers. Manag. 146 (2017) 228—243, https://doi.org/10.1016/j.enconman.2017.05.027.
[5] R.W. Serth, T.G. Lestina, Process Heat Transfer: Principles, Applications and Rules of Thumb, Elseveir Inc. Second Edition, 2014, https://doi.org/10.1016/B978-0-12-397195-1.00005-4.
[6] DeLaquill P, Kelly B, Lessley R. Investigation of thermal storage and steam generator issues, Betchel Corporation, Sandia Natl. Lab. Report SAND 93-7084 1993:1—81. doi:10.2172/10189397.
[7] J. Dersch, J. Paucar, C. Schuhbauer, A. Schweitzer, A. Stryk, Blueprint for molten salt CSP power plant, Cologne, Germany, Final report of the research project "CSP-Reference Power Plant" No. 0324253 (2021).
[8] P.A. González-Gómez, J. Gómez-Hernández, J.V. Briongos, D. Santana, Lifetime analysis of the steam generator of a solar tower plant, Appl. Therm. Eng. 159 (2019) 113805, https://doi.org/10.1016/j.applthermaleng.2019.113805.
[9] ASME. American Society of Mechanical Engineers, ASME Boiler and Pressure Vessel Code, in: Section III, Division 1, Subsection NH, 2004.
[10] P.A. González-Gómez, J. Gómez-Hernández, C. Ruiz, D. Santana, Can solar tower plants withstand the operational flexibility of combined cycle plants? Appl. Energy 314 (2022) 118951, https://doi.org/10.1016/j.apenergy.2022.118951.
[11] Q. Zhang, Z. Wang, X. Du, G. Yu, H. Wu, Dynamic simulation of steam generation system in solar tower power plant, Renew. Energy (2019) 866—876, https://doi.org/10.1016/j.renene.2018.12.064.
[12] X. Li, E. Xu, L. Ma, S. Song, L. Xu, Modeling and dynamic simulation of a steam generation system for a parabolic trough solar power plant, Renew. Energy 132 (2019) 998—1017, https://doi.org/10.1016/j.renene.2018.06.094.
[13] J. Soares, A.C. Oliveira, L. Valenzuela, A dynamic model for once-through direct steam generation in linear focus solar collectors, Renew. Energy 163 (2021) 246—261, https://doi.org/10.1016/j.renene.2020.08.127.
[14] H. Price, M. Mehos, D. Kearney, R. Cable, B. Kelly, G. Kolb, et al., Concentrating solar power best practices, Conc. Sol. Power Technol. (2021) 725—757, https://doi.org/10.1016/b978-0-12-819970-1.00020-7.
[15] D. Ferruzza, M.R. Kærn, F. Haglind, Design of header and coil steam generators for concentrating solar power applications accounting for low-cycle fatigue requirements, Appl. Energy 236 (2019) 793—803, https://doi.org/10.1016/j.apenergy.2018.12.030.
[16] ASME. American Society of Mechanical Engineers, ASME Boiler and Pressure Vessel Code, Section I, Rules for Construction of Power Boilers, 2010.
[17] European Standard EN12952-3, Water-tube Boiler and Auxiliary Installations - Part 3: Design and Calculation for Pressure Parts, 2001.
[18] D. Ferruzza, M.R. Kærn, F. Haglind, A method to account for transient performance requirements in the design of steam generators for concentrated solar power applications, Appl. Energy 269 (2020) 114931, https://doi.org/10.1016/j.apenergy.2020.114931.
[19] L. Pelagotti, K. Sørensen, T.J. Condra, A. Franco, Modelling of a coil steam generator for CSP applications, Proc 55th Int Conf Simul Model (SIMS (2014) 175—183, 2016.
[20] K. Sørensen, A. Franco, L. Pelagotti, T.J. Condra, Modelling of a cross flow evaporator for CSP application: analysis of the use of different two phase heat transfer and pressure drop correlations, Int. J. Therm. Sci. 107 (2016) 66—76, https://doi.org/10.1016/j.ijthermalsci.2016.03.025.
[21] NREL. National, Renewable Energy Laboratory, 2021. http://www.nrel.gov/csp/solarpaces/by_project.cfm. (Accessed 24 June 2021). accessed.
[22] J. Gómez-Hernández, P.A. González-Gómez, J.V. Briongos, D. Santana, Influence of the steam generator on the exergetic and exergoeconomic analysis of solar tower plants, Energy 145 (2018) 313—328, https://doi.org/10.1016/

Table A1
Correlations for molten-salt (60% NaNO$_3$ and 40% KNO$_3$) properties calculation [24].

Property	Equation
Density	$\rho(kg/m^3) = 2090 - 0.636 \cdot T(°C)$
Specific heat	$C_p(J/(kg°C)) = 1443 + 0.172 \cdot T(°C)$
Absolute viscosity	$\mu(mPa \cdot s) = 22.714 - 0.120 \cdot T(°C) + 2.281 \cdot 10^{-4} \cdot (T(°C))^2 - 1.474 \cdot 10^{-7} \cdot (T(°C))^3$
Thermal conductivity	$k(W/mK) = 0.443 + 1.9 \cdot 10^{-4} \cdot T(°C)$

j.energy.2017.12.129.

[23] W. Wagner, J.R. Cooper, A. Dittmann, J. Kijima, H.J. Kretzschmar, A. Kruse, et al., The IAPWS industrial formulation 1997 for the thermodynamic properties of water and steam, J. Eng. Gas Turbines Power 122 (2000) 150–180, https://doi.org/10.1115/1.483186.

[24] A.B. Zavoico, Solar power tower - design basis document, Sandia Natl. Lab. Report (2001), https://doi.org/10.2172/786629. SAND2001-2100.

[25] ASME. American Society of Mechanical Engineers, ASME Boiler and Pressure Vessel Code. Section II, Part D Properties, Materials, 2010.

[26] D. Anarratore, Handbook for Heat Exchangers and Tube Banks Design, Springer, Milano, Italy, 2010, https://doi.org/10.1007/978-3-642-13309-1.

[27] R. Cheesewright, P.J. Heggs, B.W. Martin, W.J. Parry, T. Ralston, Forced Convection Heat Transfer in Straight Tubes, Engineering Sciences Data Unit (ESDU), 1993.

[28] J. Taborek, Ideal tube bank correlations for heat transfer and pressure drop, in: Heat Exchanger Design Handbook, Hemisph Publ Corp, 1983, https://doi.org/10.1615/hedhme.a.000253.

[29] Y.L. Wong, D.C. Groeneveld, S.C. Cheng, Chf prediction for horizontal tubes, Int. J. Multiphas. Flow 16 (1990) 123–138, https://doi.org/10.1016/0301-9322(90)90043-I.

[30] I.E. Idel'chik, Handbook of Hydraulic Resistance. Coefficients of Local Resistance and of Friction, The U.S. Atomic Energy Commission and the National Science Foundation, Washington, D.C., 1966.

[31] G.P. Purohit, Estimating cost of shell and tube heat exchangers, Chem. Eng. 22 (1983) 56–67.

[32] B. Kelly, Advanced Thermal Storage for Central Receivers with Supercritical Coolants, Lakewood, CO, 2010, https://doi.org/10.2172/981926.

[33] NREL, National renewable energy laboratory (NREL), System Advisor Model (2020). https://sam.nrel.gov/.

[34] R.C. Byrne, Standards of the Tubular Exchangers Manufacturers Association, New York, United States, in: Tubular Exchanger Manufactures Association (TEMA), eighth ed., 1999.

[35] A.C. Caputo, P.M. Pelagagge, P. Salini, Joint economic optimization of heat exchanger design and maintenance policy, Appl. Therm. Eng. 31 (2011) 1381–1392, https://doi.org/10.1016/j.applthermaleng.2010.12.033.

[36] F. Madani Sani, S. Huizinga, K.A. Esaklul, S. Nesic, Review of the API RP 14E erosional velocity equation: origin, applications, misuses, limitations and alternatives, Wear 426–427 (2019) 620–636, https://doi.org/10.1016/j.wear.2019.01.119.

[37] T.L. Bergman, A.S. Lavine, F.P. Incropera, D.P. DeWitt, Fundamentals of Heat and Mass Transfer, seventh ed., John Wiley & Sons, Jefferson City, United States, 2011.

[38] R.S. Esfandiari, Caphter 10. Numerical Methods for Engineers and Scientists Using MATLAB®, second ed., Taylor & Francis Group, LLC, Boca Raton, Florida, 2017.

[39] R. Dooley, J. Grover, S. Paterson, M. Pearson, Electric Power Research Institue (EPRI), Evaluation of Thermal-, Creep- and Corrosion-Fatigue of Heat Recovery Steam Generator Pressure Parts, EPRI, Palo Alto, CA, 2006, 1010440.

[40] E.F. Radke, D.T. Wasyluk, D.J. Dewees, J.M. Tanzosh, Creep-fatigue design applied to molten salt solar receivers. ASME 2014 symposium on elevated temperature application of materials for fossil, Nuclear, Petrochem. Ind. (2014) 232, https://doi.org/10.1115/etam2014-1032.

[41] A. Kalnins, Twice-yield method for assessment of fatigue caused by fast thermal transient according to 2007 section VIII-division 2, Proceedings of PVP2008 (2008) 1, https://doi.org/10.1115/PVP2008-61397. –9.

[42] A. Stoppato, A. Mirandola, G. Meneghetti, E. Lo Casto, On the operation strategy of steam power plants working at variable load: technical and economic issues, Energy 37 (2012) 228–236, https://doi.org/10.1016/j.energy.2011.11.042.

[43] P.A. González-Gómez, M.R. Rodríguez-Sánchez, M. Laporte-Azcué, D. Santana, Calculating molten-salt central-receiver lifetime under creep-fatigue damage, Sol. Energy 213 (2021) 180–197, https://doi.org/10.1016/j.solener.2020.11.033.

[44] S.R. Humphries, K.U. Snowden, W. Yeung, The effect of repeated loadings on the stress relaxation properties of 2.25Cr-1Mo steel at 550°C and the influence on the Feltham "a" and "b" parameters, Mater. Sci. Eng., A 527 (2010) 3240–3244, https://doi.org/10.1016/j.msea.2010.02.011.

[45] D.L. Marriott, Isochronous stress/strain curves-origins, scope and applications, Am. Soc. Mech. Eng. Press Vessel Pip Div PVP 3 (2011) 373–379, https://doi.org/10.1115/PVP2011-57130.

[46] S. Xu, S. Jin, P Le Dreff-kerwin, Mechanical property database development and creep prediction of candidate generation IV SCWR alloys, Proc ASME (2013) 1–10, https://doi.org/10.1115/PVP2013-97290. Press Vessel Pip Conf, 2013.

[47] B. Barua, M.D. McMurtrey, R.E. Rupp, M.C. Messner, Design Guidance for High Temperature Concentrating Solar Power Components, Argonne National Laboratory, 2020, https://doi.org/10.2172/1582656.

[48] I.V.C. Becht, Elevated temperature shakedown concepts, J. Press. Vessel Technol. Trans. ASME 133 (2011) 1–5, https://doi.org/10.1115/1.4003456.

[49] D.G. Robertson, S.R. Holdsworth, Data Sheet. European Creep Collaborative Committee (ECCC), European Technology Development (ETD), 2005. https://www.eccc-creep.com/eccc-data-sheets/.

[50] D.K. Fork, J. Fitch, S. Ziaei, R.I. Jetter, Life estimation of pressurized-air solar-thermal receiver tubes, J. Sol. Energy Eng. 134 (2012) 041016, https://doi.org/10.1115/1.4007686.

[51] M.D. McMurtrey, R.E. Rupp, B. Barua, M.C. Messner, Creep-fatigue behavior and damage accumulation of a candidate structural material for CSP thermal receivers tensile testing, Idaho Natl. Lab. (2019), https://doi.org/10.2172/1562306.

[52] D.R. Eno, G.A. Young, T.-L. Sham, A unified view of engineering creep parameters, ASME 2008 Pressure Vessels Piping Conf. (2008), https://doi.org/10.1115/pvp2008-61129, 777–92.